



Publication Year	2015
Acceptance in OA @INAF	2020-06-10T07:57:03Z
Title	Relationship of dayside main layer ionosphere height to local solar time on Mars and implications for solar wind interaction influence
Authors	Zhang, Zhenfei; OROSEI, ROBERTO; Huang, Qian; Zhang, Jie
DOI	10.1002/2015JE004859
Handle	http://hdl.handle.net/20.500.12386/25977
Journal	JOURNAL OF GEOPHYSICAL RESEARCH (PLANETS)
Number	120

RESEARCH ARTICLE

10.1002/2015JE004859

Key Points:

- Local solar time affects isodensity contour height in the Martian ionosphere
- Isodensity contours around 200 km height lower by ~10 km across the local noon
- Solar wind enters the Martian ionosphere to heights ~50 km above the density peak

Correspondence to:

Z. Zhang,
zfzhang@cug.edu.cn

Citation:

Zhang, Z., R. Orosei, Q. Huang, and J. Zhang (2015), Relationship of dayside main layer ionosphere height to local solar time on Mars and implications for solar wind interaction influence, *J. Geophys. Res. Planets*, 120, 1427–1445, doi:10.1002/2015JE004859.

Received 26 MAY 2015

Accepted 24 JUL 2015

Accepted article online 29 JUL 2015

Published online 25 AUG 2015

Relationship of dayside main layer ionosphere height to local solar time on Mars and implications for solar wind interaction influence

Zhenfei Zhang¹, Roberto Orosei², Qian Huang³, and Jie Zhang¹

¹Institute of Mathematical Geology and Remote Sensing, China University of Geosciences (Wuhan), Wuhan, China, ²Istituto di Radioastronomia, Istituto Nazionale di Astrofisica, Bologna, Italy, ³Institute of Planetary Science, China University of Geosciences (Wuhan), Wuhan, China

Abstract To understand the influence of solar wind on the daytime main layer ionosphere of Mars, we investigated the local solar time (LST) variations of three characteristic heights of the ionosphere, namely, the heights of the 1 MHz and 1.5 MHz reflection points (i.e., $1.24 \times 10^{10} \text{ m}^{-3}$ and $2.79 \times 10^{10} \text{ m}^{-3}$ isodensity contours, respectively) and the density peak. We used a total of 19,996 Mars Advanced Radar for Subsurface and Ionosphere Sounding observations distributed on the northern hemisphere, with solar zenith angle $\leq 80^\circ$, acquired from June 2005 to October 2013. We exploited the kernel partial least squares regression method to extract the nonlinear relationships of the heights to LST and a few other variables. The average height of the 1 MHz reflection point decreased from ~218 km at 10:00 A.M. to ~206 km at 16:00 P.M. local time; the height of the 1.5 MHz reflection point decreased simultaneously from ~190 km to ~181 km. These decreasing trends are in contrast to the LST variation of the density peak height, which increased from ~128 km to ~137 km over the same LST interval. Based on these findings and previous results, we suggest that the solar wind may penetrate the Martian ionosphere down to altitudes of about 50 km above the main density peak and may, in conjunction with the asymmetric draping of the interplanetary magnetic field, compress the upper part of the main ionosphere layer on the P.M. side ~10 km more than on the A.M. side.

1. Introduction

The daytime Martian ionosphere is changeable with time and space, governed by dynamic solar radiation conditions, the atmospheric environment, and the crustal magnetic fields, and is influenced by solar wind and the interplanetary magnetic field (IMF). One manifestation is that the morphological characteristics of the ionosphere are observed to have certain dependence on several factors. One of the most prominent factors is the solar zenith angle (SZA), which controls the photoionization production rate of electrons and therefore controls the peak electron density magnitude and the density peak height of the main ionosphere layer. Specifically, as SZA increases from zero (at the subsolar point) to 90° (the near-terminator regions), the average peak density decreases from $\sim 1.7e + 11 \text{ m}^{-3}$ to $\sim 5.0e + 10 \text{ m}^{-3}$, and the average density peak height increases from ~130 to ~160 km; this relationship can be explained by the Chapman photoionization-recombination theory [Hantsch and Bauer, 1990; Gurnett et al., 2005; Fox and Yeager, 2006; Gurnett et al., 2008; Morgan et al., 2008; Withers, 2009; Němec et al., 2011; Zhang et al., 2015]. Another significant factor is the Martian seasons, as seasonal variations of the height of the ionosphere are observed. During the spring, the lower atmosphere is expanded because of enhanced solar heating helped by higher dust contents, and the expansion may elevate the ionospheric density peak by about 10 km [Zhang et al., 1990; Bougher et al., 2000; Zou et al., 2005; Gurnett et al., 2008; Morgan et al., 2008; Zhang et al., 2015]. The peak height is also found to be linked to Martian longitude, which is attributed to the action of the nonmigrating global thermospheric tides [Bougher et al., 2001; Seth and Jayanthi, 2008]. The crustal magnetic anomalies, distributed mainly in the southern hemisphere and low-latitude regions of the northern hemisphere [Acuña et al., 2001; Lillis et al., 2008], are found to complicate the local morphology of the ionosphere. Because of magnetic trapping of the ionospheric plasma, field-aligned “plasma cylinders” may form above the strong anomalies; along the open field lines (those connected to IMF lines), the solar wind energetic particles input may increase the density, height, and scale height of the ionosphere to form plasma bulges where the field lines are nearly vertical [Mitchell et al., 2001; Krymskii et al., 2002; Duru et al., 2006; Nielsen et al., 2007; Gurnett et al., 2008]. Besides influencing the main portion of the ionosphere (<200 km) by its energetic particles, the solar wind is considered to be a possible force generating the

observed transient, layer-like structures in the ionosphere at altitudes of around 200 km (via Kelvin-Helmholtz instabilities) [Gurnett *et al.*, 2008; Kopf *et al.*, 2008]. In the magnetic pileup region (between roughly 300–1400 km altitude), the plasma thermal pressure of the ionosphere is believed to be usually lower than the solar wind dynamic pressure, and the ionosphere is somewhat “compressed” and permeated by the solar wind-induced magnetic field [Nagy *et al.*, 2004].

In this paper, we focus on the question of whether and how the morphology of the main layer ionosphere of Mars (below ~200 km altitude) changes with local solar time (LST) if the complications caused by the crustal magnetic fields, SZA, and longitudinal variations are minimized or removed. The answer to this question could be important for further understanding of ionospheric behaviors. At higher altitudes (>275 km) it is observed that the density of the planetary ions (O^+) is higher on the duskside than on the dawnside, and this asymmetry can be explained by an asymmetric IMF draping on the two sides [Barabash *et al.*, 2007; Dubinin *et al.*, 2008; Roussos *et al.*, 2008]. Another asymmetry of the Martian ionosphere with respect to the local solar noon was observed by Safaieinili *et al.* [2007], who demonstrated that the average Chapman parameters H (neutral scale height) and N_0 (the peak electron density at the subsolar point) are significantly different when estimated (extrapolated) from the dawnside and duskside near the terminator ($SZA = 60^\circ\text{--}100^\circ$). The question remains whether the heights of the isodensity contours in the ionosphere show similar asymmetries.

In this study, we used data from the Mars Advanced Radar for Subsurface and Ionosphere Sounding (MARSIS), which is on board the European Space Agency mission Mars Express [Picardi *et al.*, 2004]. The data analyzed are limited to the northern hemisphere, where the crustal magnetic fields are weak, in order to minimize the complexity caused by the fields. Based on the selected data, we tried to reconstruct the statistical relationships of a few characteristic heights of the ionosphere (including the density peak height and heights of a few isodensity contours) to four independent variables: LST, season, latitude, and longitude. The SZA can be entirely represented by three of these factors because of the following relationship [Jacobson, 1999]:

$$\cos(SZA) = \sin L \sin D_s + \cos L \cos D_s \cos A_h, \quad (1)$$

where L is the latitude, D_s is the angle of solar declination which determines seasons, and A_h is the local hour angle. Our idea is to separate out the contribution of the LST variation from the total variability of the heights in the data (the total variability is taken as a sum of the contributions from all the independent variables). When this separation is done, we may obtain the variation trends of the heights with LST, as well as the other three variables, whereby the asymmetric distribution of heights, if any, may be seen. We exploited the kernel partial least squares (KPLS) regression method [Shawe-Taylor and Cristianini, 2004] to retrieve the trends of interest. In addition, we also gained a certain development in the data inversion technique.

The remaining parts of this paper are as follows: in section 2, the data and processing are described; in section 3, the variability of the resultant heights is displayed, and the variation regularities extracted using the KPLS method are then shown after a brief introduction of the method; in section 4, the results and their implications are discussed; and in section 5, a summary and conclusions are given.

2. Data and Processing

The MARSIS instrument and data have been described by many authors [e.g., Picardi *et al.*, 2004; Gurnett *et al.*, 2005; Jordan *et al.*, 2009; Morgan *et al.*, 2013; Zhang *et al.*, 2015]. Up to now, the data acquired from June 2005 to October 2013 have been released to the public and provide dense, comprehensive coverage of Mars. Each MARSIS observation is known as a frame, which records the time delays and intensities of the echoes of the transmitted pulses (from a 40 m tip-to-tip dipole antenna) at 160 quasi-logarithmically spaced frequencies from 0.1 to 5.5 MHz. A frame can be displayed as an ionogram, i.e., a plot of echo intensity as a function of time delay and frequency. The interesting echoes for this study are those from the vertical direction. They are usually identified visually in an ionogram [e.g., Morgan *et al.*, 2008, 2013]. Assuming a horizontally stratified ionosphere, the vertical echo has the shortest time delay for a given frequency, compared to oblique echoes. The received echo frequency (f) equals the ionospheric plasma frequency (f_p) at the reflection

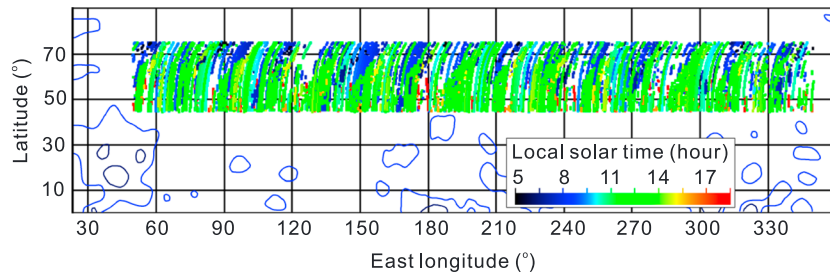


Figure 1. Spatial distribution of selected frames. The local solar time for each data point is color coded as shown in the color bar. The curves are the 12.5 (blue) and 25 nT (dark blue) isomagnitude contours of the radial component of the crustal magnetic fields at 400 km altitudes [Acuña *et al.*, 2001].

point, because an electromagnetic wave propagates in a plasma if $f > f_p$, and is reflected when $f = f_p$ [Boyd and Sanderson, 2003]. The plasma density (N , m^{-3}) is related to f_p (Hz) by

$$f_p^2 = 80.64N. \tag{2}$$

For a vertical echo, the time delay (τ , s) is determined by the distance from the radar to the reflection point and the refractive index (n) of the medium through which the wave travels, via the following equation [Boyd and Sanderson, 2003]:

$$\tau(f) = \frac{2}{c} \int_0^{z_{sc}-z} \frac{dz}{n(f,z)} = \frac{2}{c} \int_0^{z_{sc}-z} \frac{dz}{\sqrt{1 - f_p^2(z)/f^2}}, \tag{3}$$

where c is the speed of light in a vacuum ($m s^{-1}$), z is the height (m), and z_{sc} is the spacecraft height (m). By solving equation (2), the vertical density profile (density as a function of height) of the ionosphere from the spacecraft position to the density peak can be determined based on the measured (f , τ) pairs. This process is called inversion. Before inversion, data must be selected and extracted.

2.1. Data Selection and Extraction

As mentioned in the Introduction, as a first step, we selected data based on their spatial locations. The selected data are distributed between 45°N–75°N and 50°E–350°E, as displayed in Figure 1. The data are also restricted to $SZA \leq 80^\circ$ because this SZA range serves our purpose; besides, at larger SZA (approaching the terminator), the height of the ionosphere becomes more variable [e.g., Morgan *et al.*, 2008]. In Figure 1, the 12.5 and 25 nT isomagnitude contours of the radial component of the crustal magnetic field at 400 km altitude [Acuña *et al.*, 2001] are also plotted. It can be seen that the data points are in a region of weak crustal magnetic field (< 12.5 nT). In Figure 1, the data points are color coded by LST, showing that a weak correlation between LST and latitude exists in the data: LST tends to be late at lower latitudes. This may affect the interpretation of the results to some extent and will be discussed in section 4.

In Figure 1 there is a total of 19,996 data points, resulting from further selection of data within the chosen spatial and SZA region. Originally, there were about 55,800 frames in that region, from 1602 Mars Express orbits. A further selection of data is necessary because very often, the vertical echo trace in an ionogram is not entirely clear. Noise, interference of echoes from different points, and the MARSIS dipole characteristics of energy decline at low sounding frequencies may obscure the echo trace [Morgan *et al.*, 2013]. We selected ionograms based on the following three criteria:

1. The vertical echo trace is discernible at the sounding frequency of at least 1 MHz. In many ionograms, the vertical trace is invisible at frequencies lower than 1 MHz. Lowering this threshold will give an undesirably smaller sample. Augmenting the threshold will yield a larger sample, but more information about the ionosphere at higher altitudes will be lost.
2. The vertical echo trace shows a discernible cusp at its high-frequency end. The cusp is a phenomenon where the echo trace bends steeply in the direction of increasing time delay. A cusp appears because, as the sounding frequency approaches the peak ionospheric plasma frequency, the refractive index, n in equation (1), approaches zero, and the time delay increases sharply. The cusp therefore indicates the peak plasma frequency of the ionosphere.

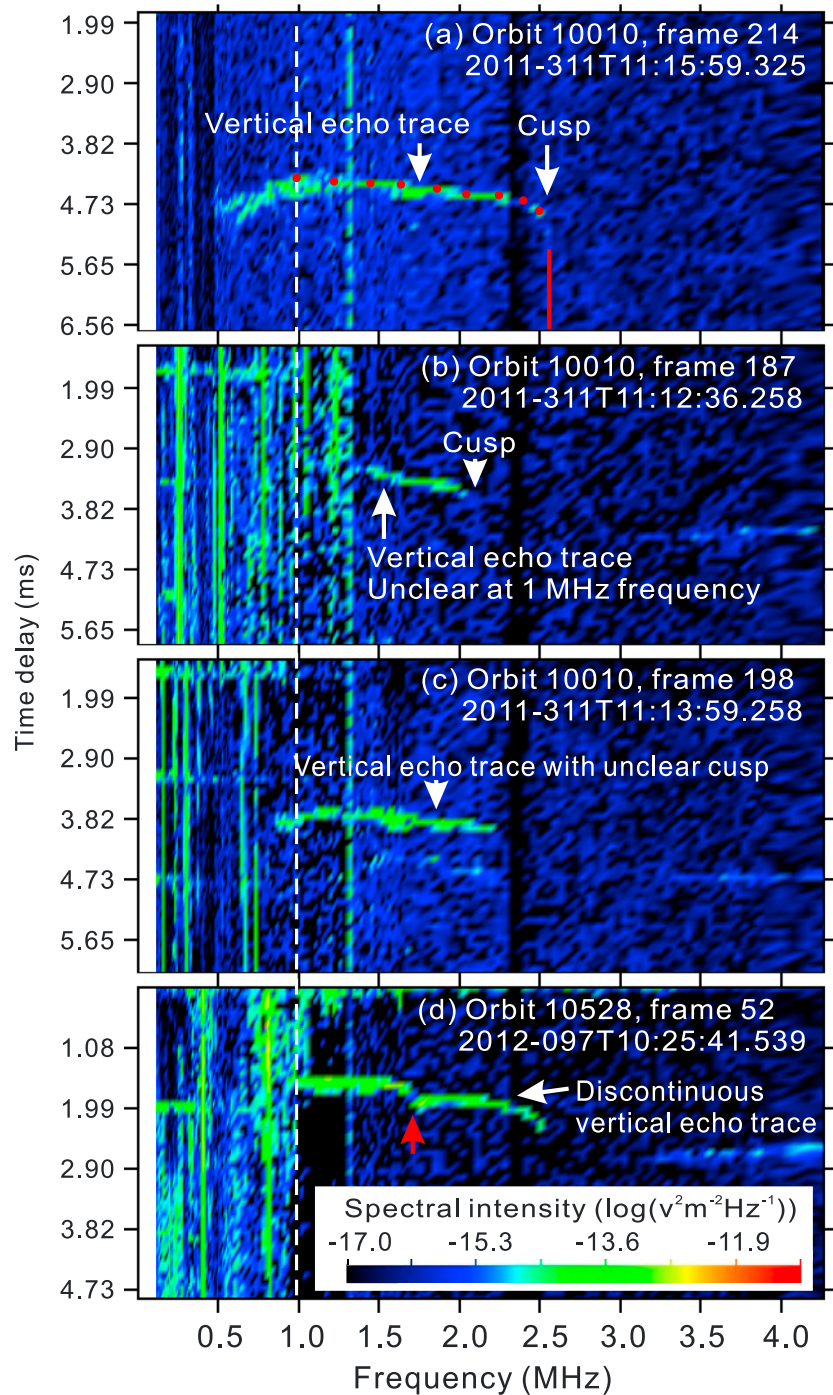


Figure 2. Examples of ionograms showing selected and eliminated data. (a) Selected data. The red dots indicate the extracted data points; the vertical red bar indicates the extracted peak plasma frequency (2.5481 MHz). The vertical dashed line indicates 1 MHz frequency positions for all four plots. (b) Eliminated because of unclear vertical echo trace at 1 MHz frequency position. (c) Eliminated because of unclear cusp of the vertical echo trace. (d) Eliminated because of discontinuous vertical echo trace. Extra cusp indicated by the red arrow represents nonmonotonic density profile.

3. The vertical echo trace must represent a monotonic density profile above the density peak up to the 1 MHz reflection position. This requires the trace to be continuous between the 1 MHz position and the cusp on the ionogram. A monotonic density profile is demanded by the lamination inversion method we apply later (section 2.2).

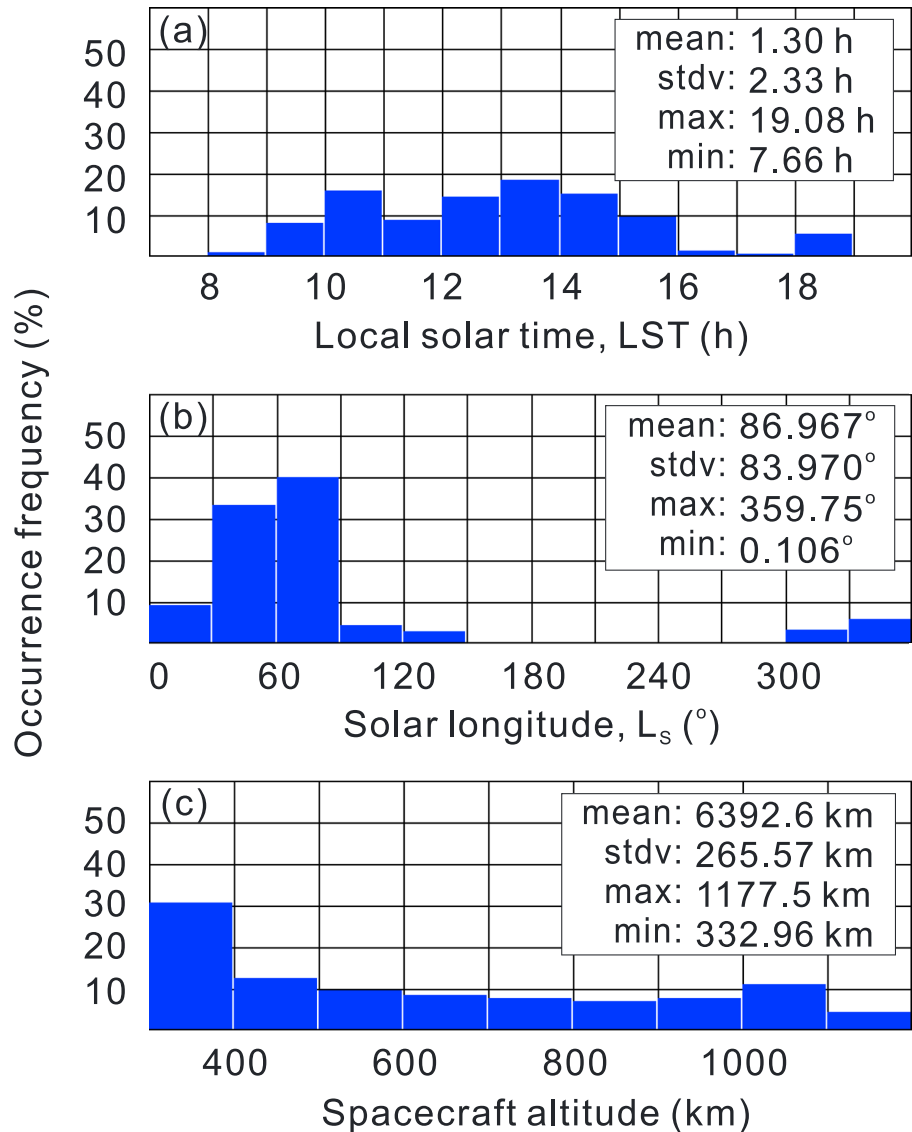


Figure 3. Occurrence frequency distributions of (a) local solar time (LST), (b) solar longitude (L_s), and (c) spacecraft altitude for all 19,996 selected frames.

Among the eliminated cases, about 90% are found to disagree with criterion (1); the rest are against either criterion (2) or (3) with roughly equal probabilities. Figure 2 illustrates examples of selected and eliminated ionograms.

Here we display a few more characteristics of the selected data relevant to subsequent study. Figure 3 shows distributions of the selected frames over LST, solar longitude (L_s), and spacecraft altitude. The data are relatively concentrated and nearly uniformly distributed between 9 and 16 h of LST (Figure 3a); the data are relatively concentrated in the northern spring-summer seasons (Figure 3b). (Note that in MARSIS data, seasons evinced by L_s : $L_s = 0^\circ, 90^\circ, 180^\circ,$ and 270° correspond to the northern spring equinox, summer solstice, autumn equinox, and winter solstice, respectively.) The data are of spacecraft altitudes between 333 and 1177 km (Figure 3c).

Data extraction means obtaining the peak plasma frequency and time delays for each sounding frequency from the vertical echo trace. The peak plasma frequency is indicated by the cusp where the trace is nearly parallel to the time delay axis, as exemplified in Figure 2a by the red vertical bar. We extracted nine, roughly evenly spaced data points on the trace, with the first one at 1 MHz (0.9951 MHz to be precise, which is one

of the center frequencies of the sounding pulses) and the others at higher frequencies, as exemplified in Figure 2a by the red dots.

2.2. Inversion

To perform the inversion, we used the lamination method, which has been expounded in detail by *Morgan et al.* [2013]; meanwhile, we added to the method an adjustment measure to better adapt our data. The entire method is described as follows.

The lamination method divides the density profile into parallel plane strata at the points where the data are taken. The method calculates the profile points step by step beginning at the lowest frequency. Each step uses the last calculated height and fits the measured time delay. The method requires the profile above the density peak to be monotonic. Our data selection criterion (3) (section 2.1) pertains to this requirement. The method also requires the in situ plasma density (at the spacecraft position) to be known or assumed [*Nielsen et al.*, 2006; *Morgan et al.*, 2013]. The in situ density may be obtained by measuring the electron plasma oscillation harmonics, which often appear in the ionogram if the spacecraft is below 600–700 km [*Duru et al.*, 2008, 2010]. However, we did not measure the oscillation harmonics; instead, we made reasonable assumptions about the in situ densities. The reasons are as follows: first, the spacecraft altitudes for our selected data are frequently (38.42%) greater than 700 km (Figure 3c). Second, it is observed that at larger altitudes (>180 km), the plasma density is more variable than at lower altitudes, as transient layers are more often seen [*Kopf et al.*, 2008; *Zhang et al.*, 2015]. For example, Figure 2a shows a layered structure at a high altitude. In this ionogram, the lower-frequency end of the vertical echo trace bends in the direction of increasing time delay, indicating an invisible cusp somewhere beyond this end. Such density variations will be neglected by the monotonic profile assumption. Regarding this assumption, a measured, accurate in situ density can be no better than an assumed value, because the real density at the beginning height may not be the smallest density in the profile if layers exist around the beginning point.

Our inversion procedure consists of two stages. The first stage is the application of the lamination technique. In this stage, for all the frames to be processed, we assumed the in situ electron density to be constant at $6.0 \times 10^6 \text{ m}^{-3}$ ($f_p \approx 0.02 \text{ MHz}$), which is a proxy for the solar wind density [*Krall and Trivelpiece*, 1973]. From the spacecraft position to the 1 MHz reflection point (which corresponds to our first data point), the density is assumed to increase exponentially to $1.24 \times 10^{10} \text{ m}^{-3}$ ($f_p \approx 1 \text{ MHz}$). Based on these assumptions, we applied the lamination inversion technique to obtain height values corresponding to each of the extracted data points.

The second stage is an adjustment of the heights calculated in the first stage. An adjustment is necessary because the spacecraft height (z_{SC}) varies over a large span (333–1177 km; Figure 3c). In this case assuming an identical in situ density, as in the first stage, is obviously not appropriate. If a fixed in situ density is assumed at different z_{SC} , then for a larger z_{SC} , the total electron content between the spacecraft position and the real reflection point may be exaggerated, and the calculated height of the reflection point may then be somewhat elevated to meet the measured time delay, leading to a nonphysical, positive dependence of the calculated heights on z_{SC} .

The adjustment procedure consists of three steps: first, we assume a fixed height value (which we call the starting height), denoted by $z_{SC,0}$, at which the $6.0 \times 10^6 \text{ m}^{-3}$ density assumption is believed to be reasonable. We assumed $z_{SC,0} = 600 \text{ km}$, considering that a plasma velocity boundary was often observed near this height [*Duru et al.*, 2010] and that steep electron density gradients were also observed around this altitude, which was considered to be the ionopause [*Duru et al.*, 2009]. Moreover, numerical simulations predicted that this height would be reasonable for the occurrence of an ionopause [e.g., *Liu et al.*, 2001]. Second, a linear function representing the z_{SC} dependence of the initially calculated heights is obtained using the least squares technique. We denote this linear function as

$$z = \phi(z_{SC}). \quad (4)$$

Third, for each data point we calculate

$$z = z' + \phi(z_{SC}) - \phi(600 \text{ km}), \quad (5)$$

where z is the adjusted height and z' is the height before adjustment.

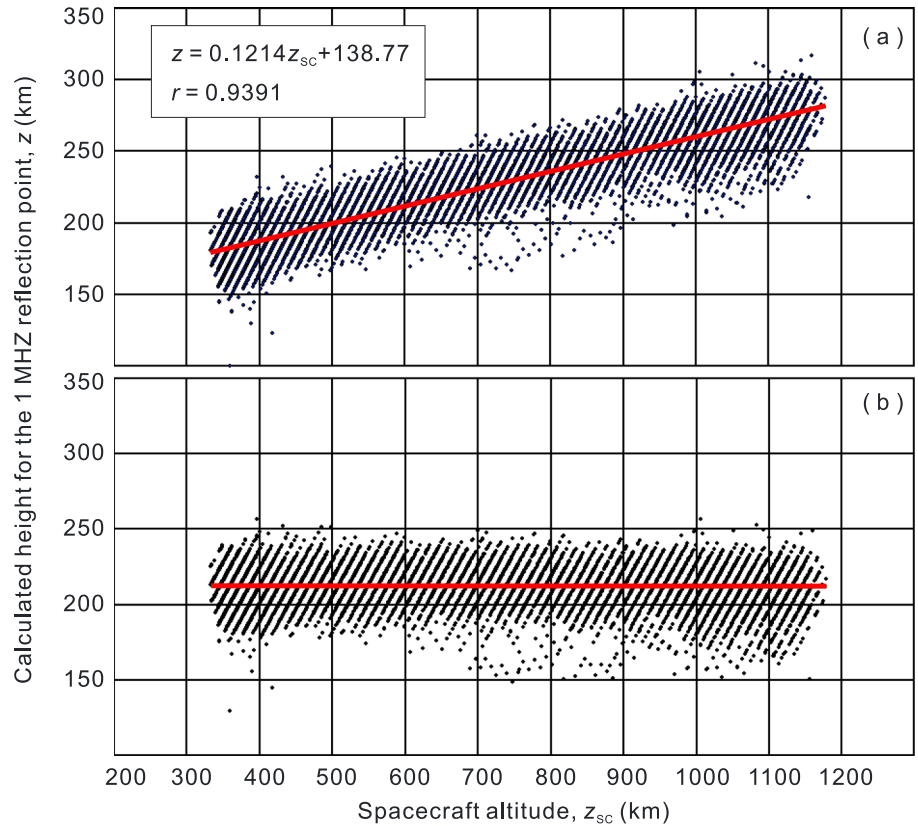


Figure 4. Inverted heights for 1 MHz reflection point for all 19,996 selected frames (a) before and (b) after adjustment. In Figures 4a and 4b, the red lines are the linear regression fit and r is the correlation coefficient.

We can show that the above adjustment method is theoretically feasible. To this end, we need only to prove that the function in equation (4) is really linear. This is equivalent to the function $\Delta z = g(\Delta z_{SC})$ being linear, where $\Delta z = z - z_0$, $\Delta z_{SC} = z_{SC} - z_{SC,0}$, and z_0 is the reflection point height calculated based on the spacecraft height $z_{SC,0}$. For simplicity, we denote the integrand in equation (3) as $\varphi(z) \equiv 1/\sqrt{1 - f_p^2(z)/f^2}$. The function $\varphi(z)$ is continuous and monotonic if $f_p(z) < f$. Based on equation (3) we have

$$\frac{2}{c} \int_{z_0 + \Delta z}^{z_{SC,0} + \Delta z_{SC}} \varphi_1(z) dz = \frac{2}{c} \int_{z_0}^{z_{SC,0}} \varphi(z) dz = \tau, \tag{6}$$

where $\varphi_1(z)$ is a function that is the same as $\varphi(z)$ in form but satisfies $\varphi_1(z_0 + \Delta z) = \varphi(z_0)$ and $\varphi_1(z_{SC,0} + \Delta z_{SC}) = \varphi(z_{SC,0})$. Let Φ_1 be the primitive of φ_1 . Then, equation (6) yields

$$\Phi_1(z_{SC,0} + \Delta z_{SC}) - \Phi_1(z_0 + \Delta z) = \tau. \tag{7}$$

Taking the derivative of equation (7) with respect to Δz_{SC} gives

$$\frac{d\Delta z}{d\Delta z_{SC}} = \frac{\partial \Phi_1(z_{SC,0} + \Delta z_{SC}) / \partial \Delta z_{SC}}{\partial \Phi_1(z_0 + \Delta z) / \partial \Delta z} = \frac{\varphi_1(z_{SC,0} + \Delta z_{SC})}{\varphi_1(z_0 + \Delta z)} = \frac{\varphi(z_{SC,0})}{\varphi(z_0)} = \text{const.} \tag{8}$$

Therefore, the function $\Delta z = g(\Delta z_{SC})$ is linear. In addition, since usually $0 < \varphi(z_{SC,0}) \ll \varphi(z_0)$, the gradient $d\Delta z/d\Delta z_{SC}$ is of a small positive value and decreases with increasing f_p of the data point to be adjusted.

Figure 4 illustrates the inverted heights of the 1 MHz reflection point (corresponding to the first data point extracted) before and after adjustment for all the selected frames. We see that before the adjustment (Figure 4a) the calculated height shows a linear dependence on the spacecraft height, and the gradient is quite small (~ 0.12). After the adjustment (Figure 4b), the dependency is removed. It is also obvious that if we had assumed a fixed starting height of, for example, 500 km instead of 600 km, then the calculated height of the 1 MHz reflection point for all the frames would be lowered systematically by a constant value of about 2.5 km. This suggests that (1) the assumption about the fixed starting height can be, to some extent, arbitrary:

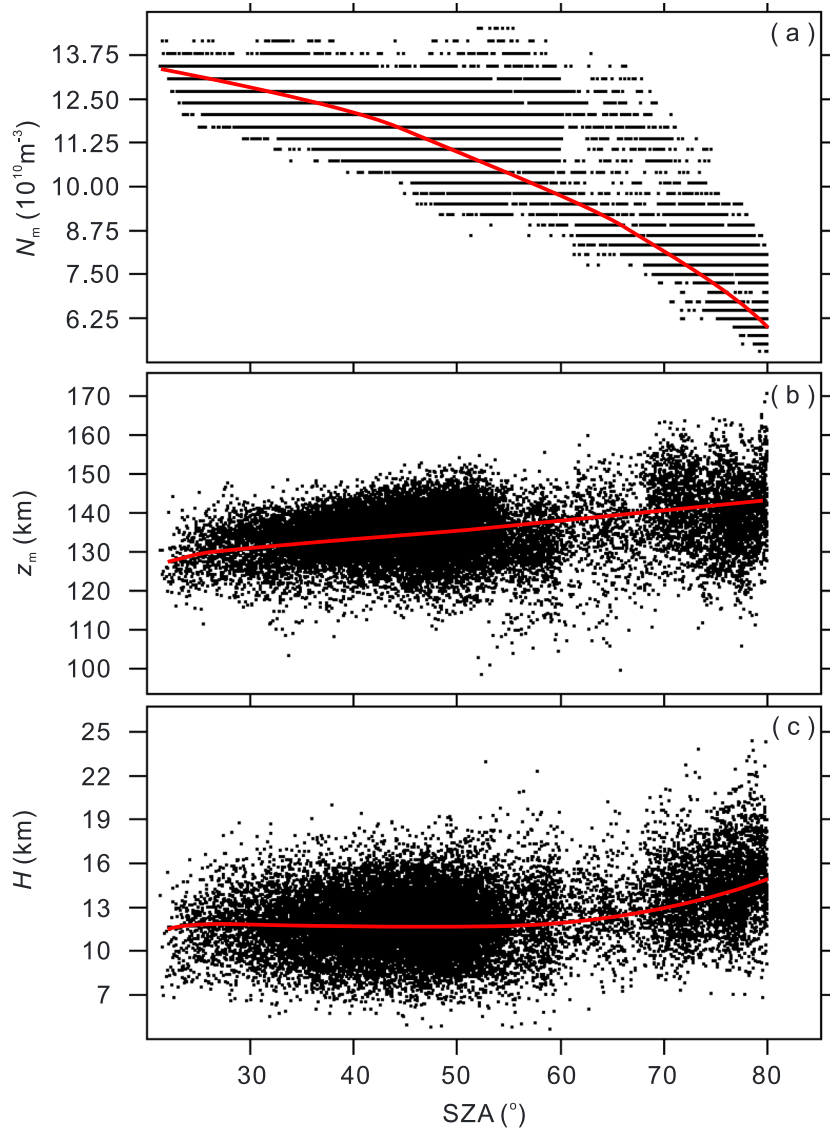


Figure 5. Scatterplot of (a) peak electron density (N_m), (b) density peak height (z_m), and (c) neutral scale height (H) against solar zenith angle (SZA) for the 19,996 selected frames. The red lines show the average values calculated in 2° SZA bins.

the height error caused by an inaccurate starting height is small if the inaccuracy is not too large; higher the sounding frequency, smaller the error; (2) comparisons between the inverted heights for different frames are not affected by the assumed value of the starting height.

For all the frames, the inversion and adjusting procedure is applied to all the data points in the same manner. In order to calculate the height of a reflection point at any frequency other than those we extracted, we need only to interpolate a data point between the extracted points, then perform the inversion.

In order to obtain the density peak height of the ionosphere, we fit the Chapman function using the inverted heights, as usual [e.g., Gurnett *et al.*, 2005; Fox and Yeager, 2006; Gurnett *et al.*, 2008; Morgan *et al.*, 2008; Withers, 2009; Němec *et al.*, 2011]. The Chapman function is

$$N = N_m \exp \left[\frac{1}{2} \left(1 - \frac{z - z_m}{H} - \exp \left(-\frac{z - z_m}{H} \right) \right) \right], \quad (9)$$

where N is the electron number density (m^{-3}), N_m is the peak density (m^{-3}), z_m is the density peak height (km), and H is the neutral scale height (km). N is related to f_p , and N_m is related to $f_{p,m}$ (the peak plasma

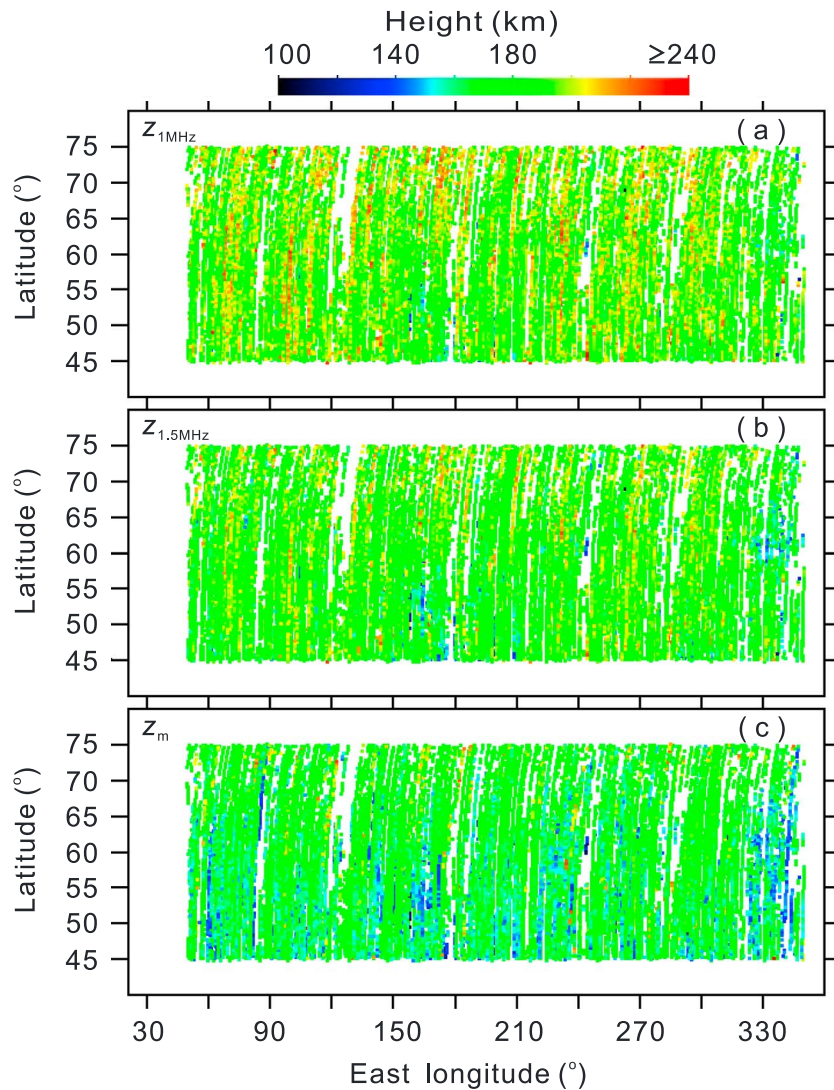


Figure 6. Scatterplots of latitude against east longitude for 19,996 selected frames. Heights of (a) 1 MHz reflection point ($z_{1\text{ MHz}}$), (b) 1.5 MHz reflection point ($z_{1.5\text{ MHz}}$), and (c) density peak (z_m) are color coded as indicated by color bar. In this figure the largest height value is 264.22 km.

frequency) by equation (2). Equation (9) can be determined in principle by two (z, f_p) pairs along with an observed $f_{p,m}$. However, we used four such pairs, which have the largest f_p values (corresponding to the rightmost four points in Figure 2a), to do the fitting, by exploiting again the least squares technique. This technique can mitigate or avoid possible ill-posed aspects of the fitting [see Zhang *et al.*, 2015, and references therein]. The remaining five heights (corresponding to the leftmost five data points in Figure 2a) are not used in the fitting, because at higher altitudes (several tens of kilometers above the density peak) where plasma transport becomes important, the density profile may deviate from a Chapman shape [e.g., Němec *et al.*, 2011].

Figures 5a–5c show, respectively, the scatterplots of the peak density (N_m), the density peak height (z_m), and the neutral scale height (H) against SZA. With SZA increasing from about 21° to 80°, the average N_m decreases from $1.3 \times 10^{11} \text{ m}^{-3}$ to $6.25 \times 10^{10} \text{ m}^{-3}$ (Figure 5a), and the average z_m increases from 128 km to about 143 km (Figure 5b). The average H is about 12 km when $\text{SZA} < 60^\circ$ and increases to about 15 km at $\text{SZA} = 80^\circ$ (Figure 5c). These variations are in agreement with previous results [see Morgan *et al.*, 2008; Withers, 2009].

3. Local Solar Time Variation of Ionospheric Heights

Based on the inverted data, in this section we considered variations of three characteristic heights (which we hereafter call “the three heights”) of the Martian ionosphere, namely, the density peak height (z_m) and heights of the 1 MHz and 1.5 MHz reflection points, denoted as $z_{1 \text{ MHz}}$ and $z_{1.5 \text{ MHz}}$ respectively. The last two are heights of $1.24 \times 10^{10} \text{ m}^{-3}$ and $2.79 \times 10^{10} \text{ m}^{-3}$ isodensity contours from equation (2). These two contours are considered to be representative of the upper part of the main layer ionosphere, relative to the lower part, which is near the density peak. In the data, between $z_{1.5 \text{ MHz}}$ and z_m , the frequency difference is at least 0.5 MHz, because the peak plasma frequency approaches ~ 2 MHz at $\text{SA} = 80^\circ$ (about $6 \times 10^{10} \text{ m}^{-3}$ in density; see Figure 5c). Our main purpose is to examine the relationships of these heights to LST. However, we also analyzed the relationships with respect to the Martian latitude, longitude, and seasons, because (1) along with LST, these factors all contribute to the variability of the heights, and all the contributions are interwoven, and (2) the relationships of these factors to z_m have been previously studied, which may serve as comparisons to our results. In the following subsection we first look at the variability of the heights with all four variables in the inverted data.

3.1. Variability of Heights in Inverted Data

Figure 6 displays the three heights in the longitude-latitude plane. In Figures 6a and 6b, no clear dependence of $z_{1 \text{ MHz}}$ and $z_{1.5 \text{ MHz}}$ on latitude and longitude can be seen. In Figure 6c, an increasing trend of z_m toward the north pole of Mars is discernible, in agreement with the result of *Morgan et al.* [2008]. This trend may reflect the SA dependence of z_m , as at higher latitudes, SA tends to be larger.

Figure 7 displays the three heights in the LST-solar longitude (L_S) plane. Because of a data gap between $L_S = 170^\circ$ and 260° , in Figure 7 the L_S values are rotated by 180° in order to avoid the gap. In this figure, the data points are distributed in “stripes,” as can be explained by equation (1) and the limited latitudinal range. The width of the stripes along the LST direction corresponds to a $30^\circ (=75^\circ-45^\circ)$ latitude interval. In Figures 7a and 7b, no clear dependence of $z_{1 \text{ MHz}}$ and $z_{1.5 \text{ MHz}}$ on LST and L_S can be seen. In Figure 7c, however, it can be seen that z_m tends to be smaller between 10:00 and 11:00 A.M. local time. This may again reflect the SA dependence of z_m , as smaller values of SA in our data are relatively concentrated at this LST interval.

Here we give an explanation why smaller SA values tend to occur in the A.M. side in our data. The phenomenon is shown in Figure 8. To explain this, we consider a very simplified situation. Suppose the spacecraft goes across the northern latitudes on a path expressed by $L = kA_h$, where $L > 0$ is the latitude, A_h is the hour angle, and k is a constant which has the same sign as A_h to guarantee $L > 0$. Furthermore, we suppose that the solar declination angle (D_S) is fixed and $k = 1$. Then, from equation (1) we have $\cos(\text{SA}) = \sin D_S \sin A_h + \cos D_S \cos^2 A_h$. Letting

$$d \cos(\text{SA})/dA_h = \sin D_S \cos A_h - 2 \cos D_S \cos A_h \sin A_h = 0, \quad (10)$$

we obtain

$$\sin A_h = \sin L = \sin D_S / (2 \cos D_S), \quad (11)$$

which indicates the latitude-time position of the maxima of $\cos(\text{SA})$ (i.e., the minima of SA). This position is on the morningside ($A_h > 0$) if $D_S > 0$ (northern spring and summer); as time changes away from noon, the position shifts along the path $\sin L = \text{const}$. Our selected data happened to be acquired mostly in the northern spring and summer (see Figures 3b and 7). The smaller values of SA are therefore relatively concentrated in the morning near noon (Figure 8).

The above inspections suggest that the relationships of the heights ($z_{1 \text{ MHz}}$, $z_{1.5 \text{ MHz}}$ and z_m) to the other variables are complicated, because of the superposition of multivariate variability. The relationship between z_m and SA, which is otherwise clear both in the data (see Figure 5b) and in theory [see, e.g., *Fox and Yeager, 2006; Withers, 2009*], is not so clear when inspected with the SA replaced by latitude, L_S , or LST (Figures 6c and 7c). It is likely that the relationships of $z_{1 \text{ MHz}}$ and $z_{1.5 \text{ MHz}}$ with LST and L_S are obscured (Figures 6a, 6b, 7a, and 7b) by the disturbances from the other variables. The relationships between the variables are mostly nonlinear. To clarify the relationships, we need a method that is capable of isolating different nonlinear aspects from the data. The kernel partial least squares (KPLS) regression is such a method, which has been expounded in detail by *Shawe-Taylor and Cristianini* [2004]. In the next subsection (section 3.2) we briefly introduce the method in the context of our application.

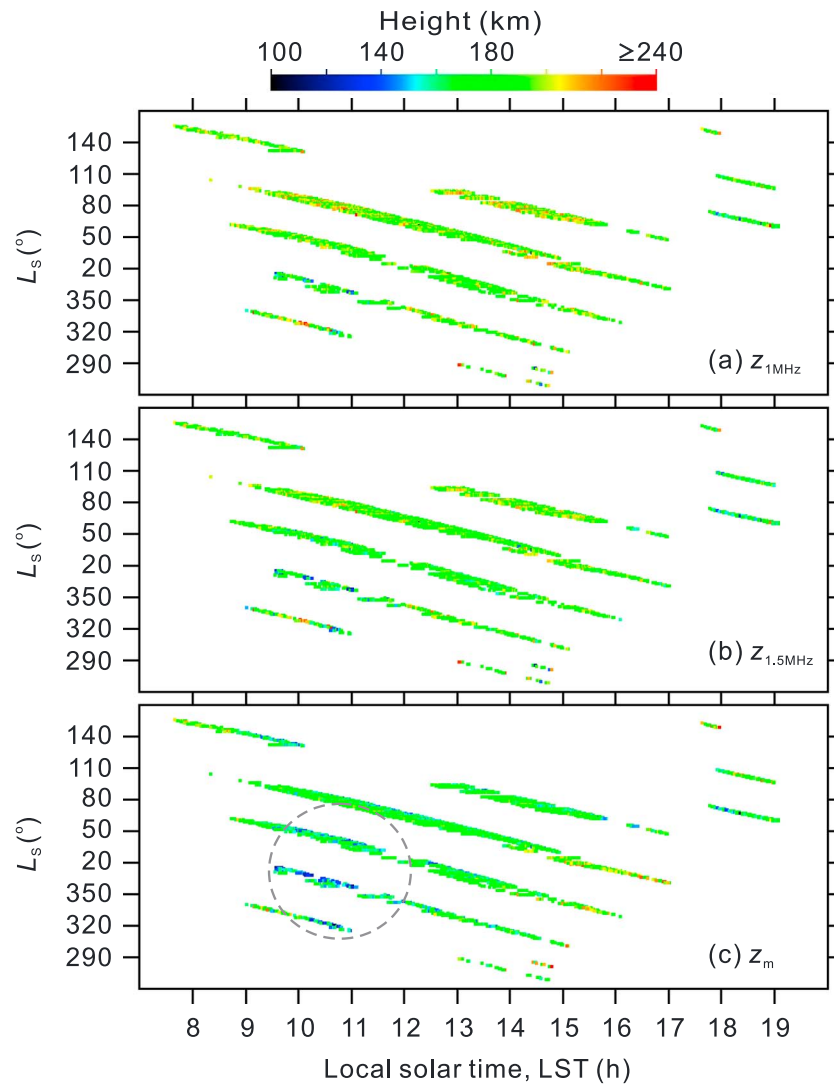


Figure 7. Scatterplots of solar longitude (L_s) against local solar time (LST) for 19,996 selected frames. Heights of (a) 1 MHz reflection point ($z_{1\text{MHz}}$), (b) 1.5 MHz reflection point ($z_{1.5\text{MHz}}$), and (c) density peak (z_m) are color coded as indicated by color bar. (In this figure the largest height value is 264.22 km.) The dashed circle in Figure 7c indicates the region where z_m is relatively small.

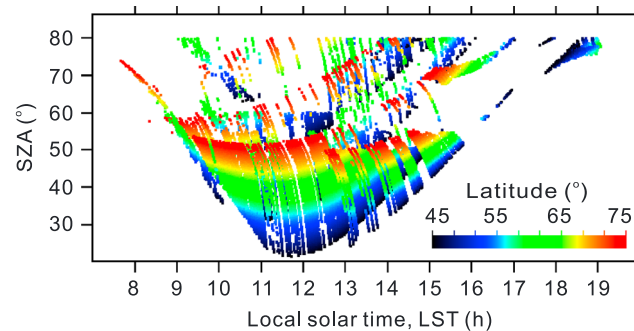


Figure 8. Scatterplots of solar zenith angle (SZA) against local solar time (LST) for 19,996 selected frames. Latitude is color coded by color bar.

3.2. KPLS Method

The kernel partial least squares (KPLS) method is an extension of the linear partial least squares (PLS) to the nonlinear domain [Shawe-Taylor and Cristianini, 2004]. PLS is a regression method used to obtain the optimal linear relationships between two groups of variables. The term optimal means that the relationship found is along the maximal covariance direction in the multivariate space. The maximal covariance direction is indicated by the singular vector corresponding to the largest singular

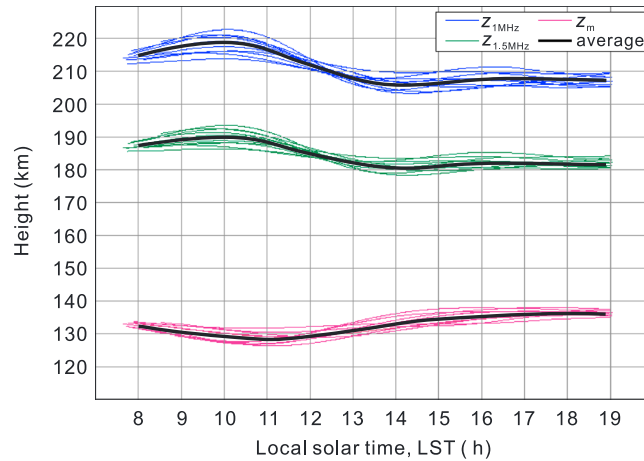


Figure 9. Relationships of heights of 1 MHz reflection point ($z_{1 \text{ MHz}}$), 1.5 MHz reflection point ($z_{1.5 \text{ MHz}}$), and density peak height (z_m) to local solar time (LST), extracted using KPSL.

value of the covariance matrix. After a relationship is extracted, the covariance matrix is projected to the space that is orthogonal to the previously obtained maximal-covariance direction, and the next relationship is then calculated in the same manner. Iterative operations will yield the desired number of relationships that are orthogonal to one another. It is well known that the regression coefficients, \mathbf{W} , can be expressed as $\mathbf{W} = (\mathbf{X}^T \mathbf{X})^{-1} \mathbf{X}^T \mathbf{Y}$, where \mathbf{X} is the data of the independent variables ($n \times p$, n is the number of samples and p is the number of independent variables) and \mathbf{Y} is the data of the dependent variables ($n \times m$, m is the number of dependent variables). The matrices $\mathbf{X}^T \mathbf{X}$ and $\mathbf{X}^T \mathbf{Y}$ are inner products of the variables,

i.e., $\mathbf{X}^T \mathbf{Y} = \langle \mathbf{X}, \mathbf{Y} \rangle$ and $\mathbf{X}^T \mathbf{X} = \langle \mathbf{X}, \mathbf{X} \rangle$. Therefore, in order to obtain \mathbf{W} , only the inner products of the variables, rather than the variables' values, are needed. The inner product of two vectors, \mathbf{x}_i and \mathbf{x}_j , or of any function of them, $\varphi(\mathbf{x}_i)$ and $\varphi(\mathbf{x}_j)$, can be replaced by a kernel function κ , i.e., $\kappa(\mathbf{x}_i, \mathbf{x}_j) = \langle \varphi(\mathbf{x}_i), \varphi(\mathbf{x}_j) \rangle$. Any function κ can be a kernel function if it is symmetric and if the matrix, $\mathbf{K} = [\kappa(\mathbf{x}_i, \mathbf{x}_j)]$, is positive semidefinite. Thus, if an appropriate $\kappa(\mathbf{x}_i, \mathbf{x}_j)$ is used to replace $\langle \mathbf{x}_i, \mathbf{x}_j \rangle$, the information in $\langle \varphi(\mathbf{x}_i), \varphi(\mathbf{x}_j) \rangle$ is automatically taken into account, while the concrete form of φ does not need to be known. If somehow the matrix $\mathbf{X}^T \mathbf{X}$ is replaced by \mathbf{K} and PLS is conducted, it can then be expected that any nonlinear relationships between \mathbf{X} and \mathbf{Y} can be obtained, because $y = \varphi(x)$ can be in any form. This is the main point of the kernel partial least squares (KPLS). The matrix \mathbf{K} is called the kernel matrix. The general algorithm for KPLS consists of the following four steps:

1. The data \mathbf{Y} is centered (i.e., each variable has zero mean), and \mathbf{X} is standardized (i.e., each variable has zero mean and unity standard deviation).
2. A kernel matrix, \mathbf{K} , is generated. The elements of \mathbf{K} are the values of a selected kernel function $\kappa(x_i, x_j)$, where x_i and x_j represent the sample values of these two variables. \mathbf{K} is an $n \times n$ symmetric matrix because κ must be a symmetric function. This step means embedding the data points into a "feature space" which is expressed by the samples of the inner products $\langle \varphi(\mathbf{x}_i), \varphi(\mathbf{x}_j) \rangle$.
3. With \mathbf{K} replacing \mathbf{X} , a procedure similar to that of PLS is run to obtain the regression coefficients, \mathbf{a} . The matrix \mathbf{a} has the same dimensions as \mathbf{Y} ($n \times m$).
4. For any new data \mathbf{X}_{new} (which has at least one row and is standardized in the same way as \mathbf{X} is), the estimates of the dependent variables $\hat{\mathbf{Y}}_{\text{new}}$ are calculated as $\hat{\mathbf{Y}}_{\text{new}} = \mathbf{K}_{\text{new}} \mathbf{a}$, where \mathbf{K}_{new} has the elements of $\kappa(\mathbf{X}_{\text{new}}, \mathbf{X})$. This step is called prediction.

In the present application, we have four independent variables ($p=4$): LST, latitude, longitude, and L_S , and three dependent variables ($m=3$): $z_{1 \text{ MHz}}$, $z_{1.5 \text{ MHz}}$, and z_m . We have a total of $n=19,996$ frames, which is too large a sample for the computations to be efficient (mainly because of the large size of the $n \times n$ kernel matrix which consumes memory storage). To avoid this difficulty, we resampled the data. We randomly (using a random number generator) selected 10 groups of samples from the entire data set, about 1000 (952–1044) samples from each group. The KPLS algorithm is then applied to each group separately. By averaging the 10 outputs, the final result is obtained. This resampling measure (called Monte Carlo cross validation [see, e.g., An et al., 2007]) facilitates the computation and enables a cross validation between the results from different subset of the data. For each group, after the regression coefficients \mathbf{a} are obtained, we used \mathbf{X} to create a new data matrix \mathbf{X}_{new} for each independent variable, in order to retrieve its relationships to the heights by prediction. For LST, for example, we let $\mathbf{X}_{\text{new}} = \mathbf{X}$. All the elements of \mathbf{X}_{new} were set to zero, but the LST column was maintained; the rows of \mathbf{X}_{new} were then sorted in an ascending order by LST to get the final form of \mathbf{X}_{new} which was used to perform the prediction step.

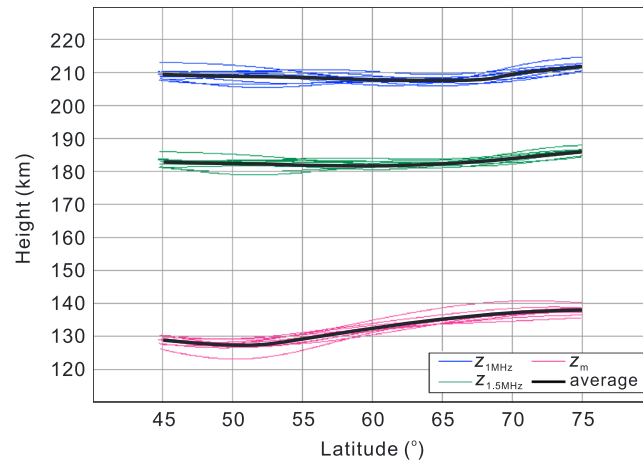


Figure 10. Relationships of heights of 1 MHz reflection point ($z_{1\text{ MHz}}$), 1.5 MHz reflection point ($z_{1.5\text{ MHz}}$), and density peak height (z_m) to latitude, extracted using KPSL.

3.3. Variations of Heights Extracted Using KPLS

Figure 9 shows the variations of the three heights with LST. In Figure 9, the relationships retrieved from each of the 10 groups of resampled data are shown as thin curves. We see that for each of the three heights ($z_{1\text{ MHz}}$, $z_{1.5\text{ MHz}}$, and z_m), the 10 curves are close to one another and have very similar trends, indicating that the ~1000 resample sizes are sufficient, and the relationships found are stable. We shall see that the trends of the heights with respect to the other parameters (latitude, longitude, and L_s) extracted using KPLS are similarly stable (Figures 10–12).

In Figure 9, it can be seen that z_m increases from ~130 km at LST = 10 h to ~137 km at LST = 16 h. This is a clearer reappearance of the trend shown in Figure 7c, which we have interpreted as being related to the SZA dependence of z_m . The most notable feature in Figure 9 is that with LST changing across the local noon, both $z_{1\text{ MHz}}$ and $z_{1.5\text{ MHz}}$ decrease distinctly, a behavior different from that of z_m . The value of $z_{1\text{ MHz}}$ decreases from ~218 km at 10:00 A.M. to ~206 km at 16:00 P.M. local time, and this height is then retained until 18:00 P.M., when the data become unavailable. Simultaneously, the value of $z_{1.5\text{ MHz}}$ decreases from

There are many options for the kernel function. In this study, we used the Gaussian form, which is

$$\kappa(\mathbf{x}_i, \mathbf{x}_j) = \exp(-\|\mathbf{x}_i - \mathbf{x}_j\|^2 / 2\sigma^2),$$

where σ is a parameter affecting the final output: a small σ (close to zero) will cause the retrieved variation trends to include too much detail in the data, thus complicating them, whereas a larger σ (close to one) may render the trends close to linear. Only one value of σ should be used for all the data, in order to make the different relationships mutually comparable. Based on tests, we choose $\sigma = 0.8$, which makes the retrieved trends of the three heights with LST monotonic over a dominantly large part of the LST range.

~190 to ~181 km, a trend similar to that of $z_{1\text{ MHz}}$. The extent of decrease of $z_{1\text{ MHz}}$ is about 3 km greater than that of $z_{1.5\text{ MHz}}$. The above variation characteristics of the three heights suggest that (1) $z_{1.5\text{ MHz}}$ and $z_{1\text{ MHz}}$ are independent of or very weakly associated with SZA, in contrast to z_m . This is consistent with the results of *Němec et al.* [2011], who observed that above ~180 km altitude, the dayside ionosphere of Mars begins to show transport-prevailing characteristics, in contrast to the dominant photoionization-recombination characteristics at lower altitudes, and (2) the upper part of the main layer ionosphere (height >180 km) is more compressed (i.e., the isodensity contours are closer to the density peak) in the local afternoon than in the local morning. We shall

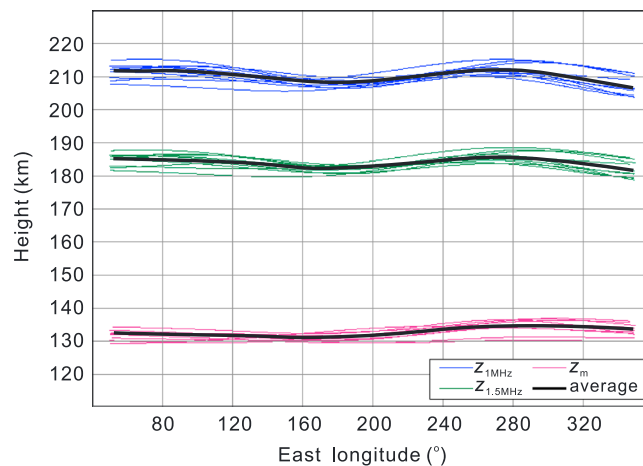


Figure 11. Relationships of heights of 1 MHz reflection point ($z_{1\text{ MHz}}$), 1.5 MHz reflection point ($z_{1.5\text{ MHz}}$), and density peak height (z_m) to longitude, extracted using KPSL.

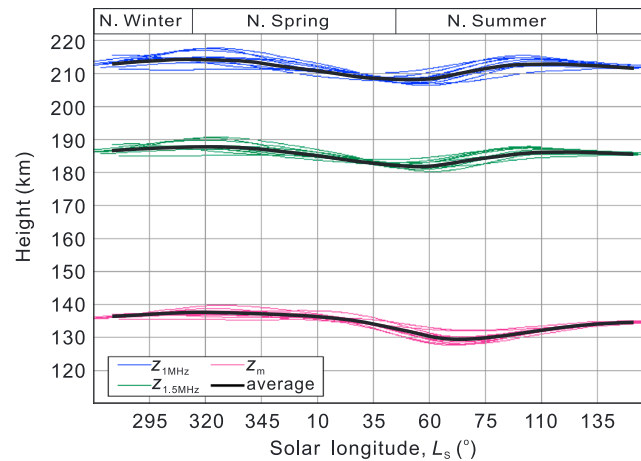


Figure 12. Relationships of heights of 1 MHz reflection point ($z_{1 \text{ MHz}}$), 1.5 MHz reflection point ($z_{1.5 \text{ MHz}}$), and density peak height (z_m) to solar longitude (L_s), extracted using KPSL.

peaks about 180° apart. The plots of $z_{1 \text{ MHz}}$ and $z_{1.5 \text{ MHz}}$ show trends similar to but more distinct than that of z_m . The wave-3 (semidiurnal wave frequency) oscillations of z_m as a function of longitude, reported by *Bougher et al.* [2001] and *Seth and Jayanthi* [2008], are not detected in the present study. What is detected in Figure 11 seems to be a wave-2 (diurnal wave frequency) oscillation. This is likely because we used a large σ value for the kernel function ($\sigma = 0.8$; see section 3.2), which is favorable for detecting larger-scale variations. It appears, in any case, that Figure 11 supports the existence of atmospheric tide effects in the Martian thermosphere. Generally, the tide-related movements prevail in the thermosphere [*Jacobson, 1999*].

In Figure 12, we see that z_m is higher by about 9 km during the northern winter-spring season than during spring-summer season. As the season advances to autumn, z_m rises again by about 6 km. The seasonal variations of z_m coincide roughly with that of the subsolar density peak height reported by *Morgan et al.* [2008]. The plots of $z_{1 \text{ MHz}}$ and $z_{1.5 \text{ MHz}}$ show seasonal trends similar to that of z_m , maybe because the ionosphere is elevated as a whole from the bottom, driven by the lower atmospheric expansion due to enhanced solar heating [e.g., *Zou et al., 2005; Zhang et al., 2015*].

4. Discussion

4.1. Interpretation of LST Variations of Ionospheric Heights

In section 3, we showed 12 relationships between the three heights and four independent variables using KPLS. The variations of z_m have been studied by many authors. In this respect, our results are in general agreement with the previous results. The heights of the isodensity contours in the upper part of the main layer ionosphere have not been specifically studied previously. Our main finding is that across the local noon, the heights of the 1.5 MHz ($z_{1.5 \text{ MHz}}$) and 1 MHz ($z_{1 \text{ MHz}}$) reflection points exhibit significantly different variations compared to that of the density peak height (z_m) (Figure 9). The value of z_m increases significantly from morning to afternoon, consistent with the SZA trends in the data (Figure 8) and predictable with the Chapman theory, whereas $z_{1.5 \text{ MHz}}$ and $z_{1 \text{ MHz}}$ decrease across the local solar noon, in agreement with the notion that at higher altitudes the ionosphere is not dominated by photo production, which closely depends on SZA. Why $z_{1.5 \text{ MHz}}$ and $z_{1 \text{ MHz}}$ show such trends, however, requires explanation. According to *Dubin et al.* [2008], the plasma fluxes in the magnetic pileup region show an asymmetry with respect to the local solar noon (stronger on the duskside than on the dawnside). They explain the asymmetry as resulting from an asymmetric draping of the IMF. They state that the draped field is stronger on the duskside than on the dawnside, because of the 56° cone angle of the field configuration, and the difference in magnetic tension may cause the plasma flux to be different on the two sides. We suggest that a similar explanation may be applicable to the heights. Although most of the in situ observed draping field strength is available at altitudes greater than about 300 km [e.g., *Brain et al., 2003; Akalin et al., 2010*], Mars Global Surveyor (MGS) detected a

discuss the possible origin of this finding later (section 4).

In Figure 10, we see that z_m increases from ~ 128 km at 45°N – 50°N to ~ 138 km at 75°N . This is a clearer reappearance of the trend shown in Figure 6c, which we have also interpreted as being related to the SZA dependence of z_m . From 45°N to about 65°N , $z_{1 \text{ MHz}}$ and $z_{1.5 \text{ MHz}}$ remain constant, but they both rise by about 4 km from 65°N to 75°N . These trends are different from that of z_m and will also be discussed in section 4.

In Figure 11, we see that z_m is ~ 2 km larger around 270°E and slightly (~ 1 km) larger around 90°E than at 180°E of the Martian longitude. It seems that the longitudinal variation of z_m has two

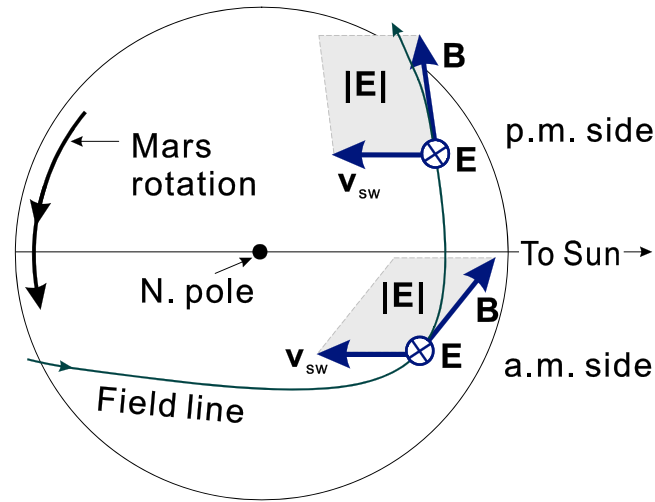


Figure 13. Sketch showing solar wind and draped interplanetary magnetic field (IMF) effect on ionospheric plasma at about 200 km height on northern hemisphere of Mars. The dark green arrowed curve represents the IMF field line, the dark blue solid arrows are the vectors, the areas of the gray parallelograms represent the magnitudes of induced electric field, and v_{sw} represents the solar wind velocity.

strong draped field of about 70 nT at ~200 km height during its aerobraking phases [Opgenoorth *et al.*, 2010]. The solar wind plasma flow may penetrate into the ionosphere at least at this height, according to the solar wind/Mars interaction dynamic model by Cloutier *et al.* [1969]. On the duskside, the stronger horizontal field may impose a stronger restriction to the upward transport of the plasma, causing decreased $z_{1.5 \text{ MHz}}$ and $z_{1 \text{ MHz}}$ on this side. Moreover, a simplified analysis of the solar wind/IMF draping configuration may show that the induced electric fields can also be different on the two sides. Figure 13 demonstrates this configuration. On the northern hemisphere of Mars, the draped field lines run from the morning-side to the afternoonside around the surface [Nagy *et al.*, 2004; Kallio *et al.*, 2008]. Behind the bow shock, the solar wind ion flow may remain at a velocity

on the order of 1 km/s in the antisun direction at altitudes below 200 km [Cloutier *et al.*, 1969; Cloutier, 1970]. The $\mathbf{v} \times \mathbf{B}$ electric field's (\mathbf{E}) magnitude is greater on the P.M. side than on the A.M. side, while its direction is downward on both sides. This \mathbf{E} field, in conjunction with magnetic trapping, is possibly capable of balancing, to some extent, the plasma thermal pressure and retarding the upward transport of ions more on the P.M. side than on the A.M. side.

According to the MGS aerobraking observations, the draped field strength begins to decrease very quickly at about 150 km height, approaching zero at about 100 km [Opgenoorth *et al.*, 2010]. Therefore, z_m , which is around 130 km, is not (or very slightly) affected by the draped field and tends to retain its SZA variation.

Based on the above analysis, we conclude that the influence of the IMF draped magnetic field on the ionosphere may reach altitudes of about 50 km above the density peak or lower. On the P.M. side, the ionosphere is about 10 km more compressed than it is on the A.M. side. Since IMF is carried by the solar wind, we may infer that the solar wind may penetrate into the Martian ionosphere down to the same low altitudes.

According to the numerical simulations by Kallio *et al.* [2008], at high latitudes the draped field lines may be less frequent at lower altitude than at low latitudes (e.g., at low latitudes the IMF lines “wrap” the planet sphere, while directly above the north pole they are straight lines tangent to the sphere). In other words, at high latitudes the draped field lines tend to occur at higher altitudes. This may be related to the increasing trends of $z_{1.5 \text{ MHz}}$ and $z_{1 \text{ MHz}}$ with increasing latitude at high latitudes (>65°; Figure 10).

4.2. Further Remarks on Results

In the above subsection (section 4.1) we attempted to present a qualitative explanation of the height variation regularities found. The explanation is open because of the complexity of the issue. However, the statistically extracted variation trends of the heights are essentially reliable because they are based on a large data set. The KPLS method has been tuned (by adjusting the σ parameter) to favor the extraction of large-scale features, which reduces difficulty in the analysis. As we are focused on “trends” rather than details of the height variability, many factors may be neglected without much affecting the results. For example, we ignored the changes in the solar UV radiation strength due to rotation of the Sun, which may cause day-to-day oscillations of the Martian ionospheric peak density [e.g., Breus *et al.*, 2004; Withers and Mendillo, 2005]. Such agents may be responsible for the spread of the heights around their average trends.

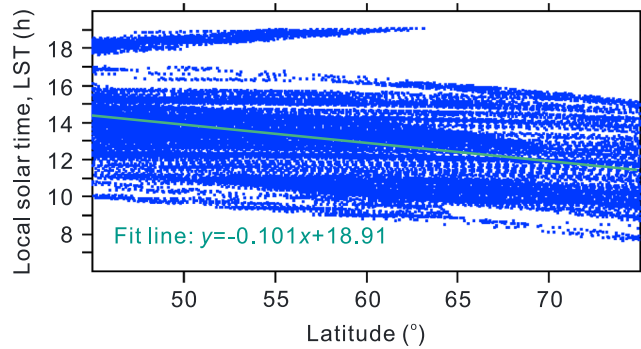


Figure 14. Scatterplot of local solar time (LST) against latitude for the 19,996 selected frames, showing weak correlation between the two variables.

Are the “independent” variables, which we have considered, really independent of one another? Dependencies between the argument variables may in general render the interpretation uncertain, because the variance contributions from mutually correlated variables are inseparable by KPLS. In this regard, the most considerable is that, as mentioned in section 2.1, LST is somewhat linked to latitude. This is further clarified in Figure 14, whereby a weak, negative correlation between LST and latitude

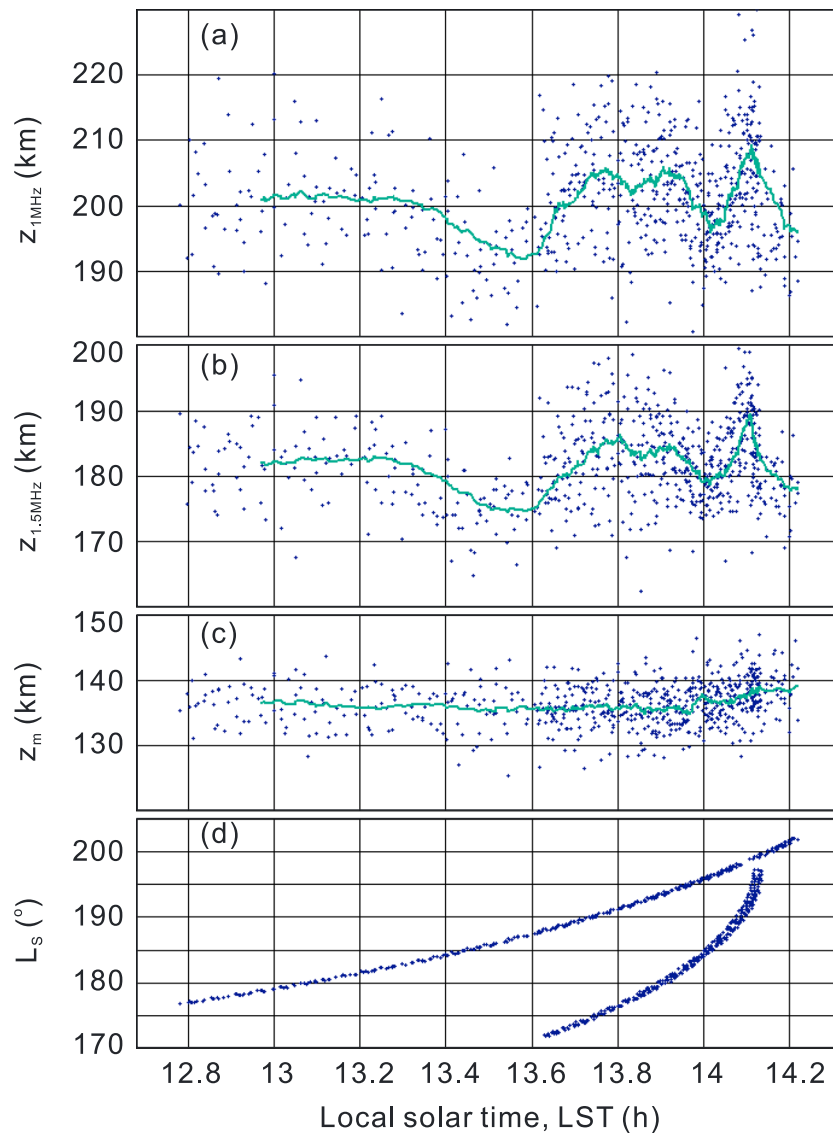


Figure 15. Scatterplot of height of (a) the 1 MHz reflection point ($z_{1\text{ MHz}}$), (b) 1.5 MHz reflection point ($z_{1.5\text{ MHz}}$), (c) electron density peak (z_m), and (d) solar longitude (L_S) against the local solar time (LST), extracted from 672 MGS RS electron density profiles [Tyler et al., 2006]. The green curves in Figures 15a–15c indicate 30-point running window averages.

can be perceived. However, the dependency in Figure 14 does not affect the results. If, for instance, the largest values of $z_{1.5 \text{ MHz}}$ and $z_{1 \text{ MHz}}$ are partially due to higher latitudes, this does not contradict the LST dependence of these heights nor modify the interpretations in section 4.1.

In order to examine the extracted LST variation trends, we also inspected the MGS radio science (RS) data [Tyler *et al.*, 2006]. Among the total of 5126 MGS electron density profiles, 672 are within our chosen latitude, longitude, SZ, and LST scope. From each of these profiles, we extracted the $z_{1.5 \text{ MHz}}$, $z_{1 \text{ MHz}}$, and z_m , as shown in Figure 15. Note that before the extraction of $z_{1.5 \text{ MHz}}$ and $z_{1 \text{ MHz}}$, a five-point running window average is conducted for each of the profiles, because at high altitudes ($>180 \text{ km}$) the electron density usually changes severely with height. From Figure 15, we see that between 12 and 13.6 h local solar time, $z_{1 \text{ MHz}}$ (Figure 15a) and $z_{1.5 \text{ MHz}}$ (Figure 15b) exhibit decreasing trends with LST, while z_m remains constant (Figure 15c). These seem to resemble those in Figure 9, where $z_{1 \text{ MHz}}$ and $z_{1.5 \text{ MHz}}$ decrease across the local noon while z_m does not. After 13.6 h, $z_{1 \text{ MHz}}$ and $z_{1.5 \text{ MHz}}$ appear to be irregular. The cause of these irregularities is unclear, but they may be related to the large seasonal scope involved (shown in Figure 15d). Since these MGS data were acquired in local seasons that are different from those of our selected MARSIS data (cf. Figure 12), further analysis is not attempted here.

5. Summary and Conclusions

Based on the MARSIS active ionosphere sounding data, we investigated the variation regularities of the $1.24 \times 10^{10} \text{ m}^{-3}$ and $2.79 \times 10^{10} \text{ m}^{-3}$ isodensity contours (corresponding to the 1 MHz and 1.5 MHz reflection points, respectively) and the density peak of the daytime main layer ionosphere of Mars. We used the kernel partial least squares regression method to extract nonlinear relationships of the heights with changing local solar time (LST) and three other factors, namely, the Martian latitude, longitude, and seasons. We found that the average height of the 1 MHz reflection point decreases from $\sim 218 \text{ km}$ at 10:00 A.M. local time to $\sim 206 \text{ km}$ at 16:00 P.M., and simultaneously, the height of the 1.5 MHz reflection point decreases from $\sim 190 \text{ km}$ to $\sim 181 \text{ km}$. These decreasing trends with LST are in prominent contrast to the LST variation of the density peak height, which increases from $\sim 128 \text{ km}$ to $\sim 137 \text{ km}$ over the same local time interval. For these findings, we suggest a physical explanation inspired by one of the previously observed asymmetric distributions of ion flux at larger altitudes ($>270 \text{ km}$) [e.g., Dubinin *et al.*, 2008]. We suggest that the solar wind may penetrate into the Martian ionosphere down to altitudes of about 50 km above the main density peak. The solar wind, in conjunction with the asymmetric draping of the interplanetary magnetic field (IMF) across the local solar noon, may compress the upper part (around 200 km height) of the main layer ionosphere on the P.M. side more than on the A.M. side. This explanation is in accordance with the dynamic solar wind/Mars interaction model proposed by Cloutier *et al.* [1969]. Concerning the heights of the 1 MHz and 1.5 MHz reflection points, we also show that (1) their longitudinal distributions show two peaks $\sim 180^\circ$ apart, probably a diurnal oscillation driven by the nonmigrating atmospheric tides; (2) their latitudinal distributions are constant between latitudes of 45° – 65° but increased by about 4 km at higher latitudes ($>65^\circ$); and (3) their seasonal variations are similar to that of the density peak height, which is relatively high in the northern spring, in general agreement with the existing notion that the ionosphere may be elevated in bulk by enhanced solar heating of the lower atmosphere. For inversion of the height profile of the ionosphere from the MARSIS measurements, we developed an adjustment technique on the basis of the existing lamination method. The adjustment technique may facilitate the inversion in situations where the in situ plasma densities are unavailable, the real profiles are not monotonic, and a large range of spacecraft height is involved when a large number of measurements must be processed.

Acknowledgments

MARSIS data were jointly generated by the Italian Space Agency and NASA. MGS RS data were generated by NASA. These data are published by the NASA Planetary Data System and are freely available through the NASA PDS Geosciences Node (<http://pds-geosciences.wustl.edu/missions/>). This work was funded by the Natural Science Foundation of China (project 41274181 and 40874092). We would like to thank the two reviewers for their suggestions to improve this manuscript.

References

- Acuña, M. H., *et al.* (2001), Magnetic field of Mars: Summary of results from the aerobraking and mapping orbits, *J. Geophys. Res.*, *106*(E10), 23,403–23,417, doi:10.1029/2000JE001404.
- Akalin, F., D. D. Morgan, D. A. Gurnett, D. L. Kirchner, D. A. Brain, R. Modolo, M. H. Acuña, and J. R. Easley (2010), Dayside induced magnetic field in the ionosphere of Mars, *Icarus*, *206*, 104–111, doi:10.1016/j.icarus.2009.03.021.
- An, S., W. Liu, and S. Venkatesh (2007), Fast cross-validation algorithms for least squares support vector machine and kernel ridge regression, *Pattern Recognit.*, *40*, 2154–2162, doi:10.1016/j.patcog.2006.12.015.
- Barabash, S., A. Fedorov, R. Lundin, and J. A. Sauvaud (2007), Martian atmospheric erosion rates, *Science*, *315*(5811), 501–503, doi:10.1126/science.1134358.
- Bougher, S. W., S. Engel, R. G. Roble, and B. Foster (2000), Comparative terrestrial planet thermospheres: 3. Solar cycle variation of global structure and winds at solstices, *J. Geophys. Res.*, *105*, 17,669–17,692, doi:10.1029/1999JE001232.

- Bougher, S. W., S. Engel, D. P. Hinson, and J. M. Forbes (2001), Mars Global Surveyor Radio Science electron density profiles: Neutral atmosphere implications, *Geophys. Res. Lett.*, *28*, 3091–3094, doi:10.1029/2001GL012884.
- Boyd, T. J. M., and J. J. Sanderson (2003), *The Physics of Plasmas*, Cambridge Univ. Press, New York.
- Brain, D. A., F. Bagenal, M. H. Acuña, and J. E. P. Connerney (2003), Martian magnetic morphology: Contributions from the solar wind and crust, *J. Geophys. Res.*, *108*(A12), 1424, doi:10.1029/2002JA009482.
- Breus, T. K., A. M. Krymskii, D. H. Crider, N. F. Ness, D. Hinson, and K. K. Barashyan (2004), Effect of the solar radiation in the topside atmosphere/ionosphere of Mars: Mars Global Surveyor observations, *J. Geophys. Res.*, *109*, A09310, doi:10.1029/2004JA010431.
- Cloutier, P. A. (1970), Dynamics of the interaction of the solar wind with a planetary atmosphere, *Radio Sci.*, *5*(2), 387–389, doi:10.1029/R5005i002p00387.
- Cloutier, P. A., M. B. McElroy, and F. C. Michel (1969), Modification of the Martian ionosphere by the solar wind, *J. Geophys. Res.*, *74*(26), 6215–6228, doi:10.1029/JA074i026p06215.
- Dubinin, E., G. Chanteur, M. Fraenz, R. Modolo, J. Woch, E. Roussos, S. Barabash, R. Lundin, and J. D. Winningham (2008), Asymmetry of plasma fluxes at Mars. ASPERA-3 observations and hybrid simulations, *Planet. Space Sci.*, *56*, 832–835, doi:10.1016/j.pss.2007.12.006.
- Duru, F., D. A. Gurnett, T. F. Averkamp, D. L. Kirchner, R. L. Huff, A. M. Persoon, J. J. Plaut, and G. Picardi (2006), Magnetically controlled structures in the ionosphere of Mars, *J. Geophys. Res.*, *111*, A12204, doi:10.1029/2006JA011975.
- Duru, F., D. A. Gurnett, D. D. Morgan, R. Modolo, A. F. Nagy, and D. Najib (2008), Electron densities in the upper ionosphere of Mars from the electron plasma oscillations, *J. Geophys. Res.*, *113*, A07302, doi:10.1029/2008JA013073.
- Duru, F., D. A. Gurnett, R. A. Frahm, J. D. Winningham, D. D. Morgan, and G. G. Howes (2009), Steep, transient density gradients in the Martian ionosphere similar to the ionopause at Venus, *J. Geophys. Res.*, *114*, A12310, doi:10.1029/2009JA014711.
- Duru, F. D. A., J. D. Gurnett, R. Winningham, R. Frahm, and R. Modolo (2010), A plasma flow velocity boundary at Mars from the disappearance of electron plasma oscillations, *Icarus*, *206*, 74–82, doi:10.1016/j.icarus.2009.04.012.
- Fox, J. L., and K. E. Yeager (2006), Morphology of the near-terminator Martian ionosphere: A comparison of models and data, *J. Geophys. Res.*, *111*, A10309, doi:10.1029/2006JA011697.
- Gurnett, D. A., et al. (2005), Radar soundings of the ionosphere of Mars, *Science*, *310*, 1929–1933, doi:10.1126/science.1121868.
- Gurnett, D. A., et al. (2008), An overview of radar soundings of the Martian ionosphere from the Mars Express spacecraft, *Adv. Space Res.*, *41*, 1335–1346, doi:10.1016/j.asr.2007.01.062.
- Hantsch, M. H., and S. J. Bauer (1990), Solar control of the Mars ionosphere, *Planet. Space Sci.*, *38*, 539–542.
- Jacobson, M. Z. (1999), *Fundamentals of Atmospheric Modeling*, Cambridge Univ. Press, New York.
- Jordan, R., et al. (2009), The Mars express MARSIS sounder instrument, *Planet. Space Sci.*, *57*, 1975–1986, doi:10.1016/j.pss.2009.09.016.
- Kallio, E., R. A. Frahm, Y. Futaana, A. Fedorov, and P. Janhunen (2008), Morphology of the magnetic field near Mars and the role of the magnetic crustal anomalies: Dayside region, *Planet. Space Sci.*, *56*, 852–855, doi:10.1016/j.pss.2007.12.002.
- Kopf, A. J., D. A. Gurnett, D. D. Morgan, and D. L. Kirchner (2008), Transient layers in the topside ionosphere of Mars, *Geophys. Res. Lett.*, *35*, L17102, doi:10.1029/2008GL034948.
- Krall, N. A., and A. W. Trivelpiece (1973), *Principles of Plasma Physics*, McGraw-Hill Book Company, New York.
- Krymskii, A. M., T. K. Breus, N. F. Ness, M. H. Acuña, J. E. P. Connerney, D. H. Crider, D. L. Mitchell, and S. J. Bauer (2002), Structure of the magnetic field fluxes connected with crustal magnetization and topside ionosphere at Mars, *J. Geophys. Res.*, *107*(A9), 1245, doi:10.1029/2001JA000239.
- Lillis, R. J., H. V. Frey, M. Manga, D. Mitchell, R. Lin, M. Acuna, and S. Bougher (2008), An improved crustal magnetic field map of Mars from electron reflectometry: Highland volcano magmatic history and the end of the Martian dynamo, *Icarus*, *194*, 575–596, doi:10.1016/j.icarus.2007.09.032.
- Liu, Y., A. E. Nagy, T. I. Gombosi, D. L. DeZeeuw, and K. G. Powell (2001), The solar wind interaction with Mars: Results of three-dimensional three-species MHD studies, *Adv. Space Res.*, *27*(11), 1837–1846, doi:10.1016/S0273-1177(01)00301-5.
- Mitchell, D. L., R. P. Lin, C. Mazelle, H. Reme, P. A. Cloutier, J. E. P. Connerney, M. H. Acuna, and N. F. Ness (2001), Probing Mars' crustal magnetic field and ionosphere with the MGS Electron Reflectometer, *J. Geophys. Res.*, *106*(E10), 23,419–23,427, doi:10.1029/2000JE001435.
- Morgan, D. D., D. A. Gurnett, D. L. Kirchner, J. L. Fox, E. Nielsen, and J. J. Plaut (2008), Variation of the Martian ionospheric electron density from Mars Express radar soundings, *J. Geophys. Res.*, *113*, A09303, doi:10.1029/2008JA013313.
- Morgan, D. D., O. Witasse, E. Nielsen, D. A. Gurnett, F. Duru, and D. L. Kirchner (2013), The processing of electron density profiles from the Mars Express MARSIS topside sounder, *Radio Sci.*, *48*, 1–11, doi:10.1002/rds.20023.
- Nagy, A. F., et al. (2004), The plasma environment of Mars, *Space Sci. Rev.*, *111*, 33–114, doi:10.1023/B:SPAC.0000032718.47512.92.
- Němec, F., D. D. Morgan, D. A. Gurnett, F. Duru, and V. Truhlik (2011), Dayside ionosphere of Mars: Empirical model based on data from the MARSIS instrument, *J. Geophys. Res.*, *116*, E07003, doi:10.1029/2010JE003789.
- Nielsen, E., H. Zou, D. A. Gurnett, D. L. Kirchner, D. D. Morgan, R. Huff, R. Orosei, A. Safaeinili, J. J. Plaut, and G. Picardi (2006), Observations of vertical reflections from the topside Martian ionosphere, *Space Sci. Rev.*, *126*, 373–388, doi:10.1007/978-0-387-70943-7_15.
- Nielsen, E., X.-D. Wang, D. A. Gurnett, D. L. Kirchner, R. Huff, R. Orosei, A. Safaeinili, J. J. Plaut, and G. Picardi (2007), Vertical sheets of dense plasma in the topside Martian ionosphere, *J. Geophys. Res.*, *112*, E02003, doi:10.1029/2006JE002723.
- Opgenoorth, H. J., R. S. Dhillon, L. Rosenqvist, M. Lester, N. J. T. Edberg, S. E. Milan, P. Withers, and D. Brain (2010), Day-side ionospheric conductivities at Mars, *Planet. Space Sci.*, *58*, 1139–1151, doi:10.1016/j.pss.2010.04.004.
- Picardi, G., et al. (2004), MARSIS: Mars Advanced Radar for Subsurface and Ionosphere Sounding, in *Mars Express: A European Mission to The Red Planet*, SP-1240, edited by A. Wilson, pp. 51–70, Eur. Space Agency Publ. Div., Noordwijk, Netherlands.
- Roussos, E., M. Fränz, E. Dubinin, C. Martinecz, J. Woch, U. Motschmann, J. D. Winningham, R. A. Frahm, S. Barabash, and R. Lundin (2008), Energetic electron asymmetries at Mars: ASPERA-3 observations, *Planet. Space Sci.*, *56*, 836–839, doi:10.1016/j.pss.2007.12.009.
- Safaeinili, A., W. Kofman, J. Mouginot, Y. Gim, A. Herique, A. B. Ivanov, J. J. Plaut, and G. Picardi (2007), Estimation of the total electron content of the Martian ionosphere using radar sounder surface echoes, *Geophys. Res. Lett.*, *34*, L23204, doi:10.1029/2007GL032154.
- Seth, S. P., and U. B. Jayanthi (2008), Longitudinal distribution of thermospheric densities and ionization rates in the upper atmosphere of Mars at mid-latitude using MGS ACC data, *Adv. Space Res.*, *41*, 1353–1360, doi:10.1016/j.asr.2007.05.056.
- Shawe-Taylor, J., and N. Cristianini (2004), *Kernel Methods for Pattern Analysis*, pp. 176–193, Cambridge Univ. Press, New York.
- Tyler, G. L., et al. (2006), MGS RST Science Data Products (Editor: R.A. Simpson), NASA Planetary Data System. [Available at ftp://pds-geosciences.wustl.edu/mgs/mgs-m-rss-5-sdp-v1.]
- Withers, P. (2009), A review of observed variability in the dayside ionosphere of Mars, *Adv. Space Res.*, *44*, 277–307, doi:10.1016/j.asr.2009.04.027.

- Withers, P., and M. Mendillo (2005), Response of peak electron densities in the Martian ionosphere to day-to-day changes in solar flux due to solar rotation, *Planet. Space Sci.*, *53*, 1401–1418, doi:10.1016/j.pss.2005.07.010.
- Zhang, M. H. G., J. G. Luhmann, and A. J. Kliore (1990), A post-Pioneer Venus reassessment of the Martian dayside ionosphere as observed by radio occultation methods, *J. Geophys. Res.*, *95*, 14,829–14,839, doi:10.1029/JB095iB09p14829.
- Zhang, Z., R. Orosei, Q. Huang, and J. Zhang (2015), Topside of the Martian ionosphere near the terminator: Variations with season and solar zenith angle and implications for the origin of the transient layers, *Icarus*, *251*, 12–25, doi:10.1016/j.icarus.2014.09.036.
- Zou, H., J.-S. Wang, and E. Nielsen (2005), Effect of the seasonal variations in the lower atmosphere on the altitude of the ionospheric main peak at Mars, *J. Geophys. Res.*, *110*, A09311, doi:10.1029/2004JA010963.